CHEMISTRY OF MATERIALS

ARTICLE

pubs.acs.org/cm

Oxygen-Vacancy-Related Structural Phase Transition of $Ba_{0.8}Sr_{0.2}Co_{0.8}Fe_{0.2}O_{3-\delta}$

Zhèn Yáng,*[†] Julia Martynczuk,[†] Konstantin Efimov,[‡] Ashley S. Harvey,[†] Anna Infortuna,[†] Peter Kocher,[†] and Ludwig J. Gauckler[†]

[†]Nonmetallic Inorganic Materials, Department of Materials, ETH Zurich, 8093 Zurich, Switzerland

[‡]Institute of Physical Chemistry and Electrochemistry, Leibniz Universitaet Hannover, D-30167 Hannover, Germany

ABSTRACT: $Ba_{0.8}Sr_{0.2}Co_{0.8}Fe_{0.2}O_{3-\delta}$ exists as a single cubic phase at 1000 °C in air. Upon slow cooling, it transforms, between 900 and 700 °C, to a mixture of cubic, hexagonal, and rhombohedral phases, as evidenced by X-ray diffraction and transmission electron microscopy. The reversible phase change is accompanied by a large change of the oxygen content ($\Delta\delta = 0.14$) of $Ba_{0.8}Sr_{0.2}Co_{0.8}Fe_{0.2}O_{3-\delta}$ and a volume change of 1.2 vol% at 700−900 °C. The multiphase material shows lamellar shaped structures in the HRTEM micrographs due to the partial transformation of the material from the cubic to the hexagonal and rhombohedral symmetries. The electrical conductivity changes from *p*-type semiconductivity between room temperature and 700 °C to metal-like conductivity at higher temperatures up to 1000 °C. The electrical conductivity is irreversibly changed upon thermal cycling due to the formation of microcracks.

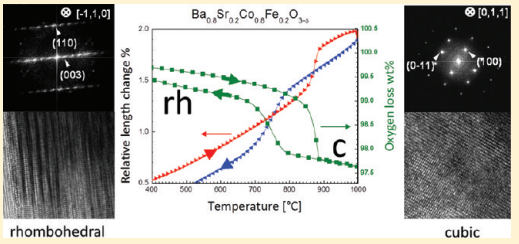

KEYWORDS: BSCF, phase transition, X-ray diffraction, transmission electron microscopy, electrical conductivity, thermal expansion coefficient, mixed ionic-electronic conductor, perovskite

1. INTRODUCTION

Perovskite-type materials have been widely studied in recent decades because of their multiple functional properties in electrical, optical, and magnetic applications.[1,2] Some of the perovskite-type materials have been studied for their good oxygen catalytic activity, high electrical conductivity, and required oxygen ionic conductivity, especially as cathodes in the field of the solid oxide fuel cell (SOFC)[3,4] and oxygen permeation membranes.[5] One perovskite-type composition $Ba_{0.5}Sr_{0.5}Co_{0.8}Fe_{0.2}O_{3-\delta}$ of the family of the more general system $Ba_xSr_{1-x}Co_yFe_{1-y}O_{3-\delta}$ (BSCF) was reported for the first time in 2000 as an oxygen permeation ceramic membrane material[6] and in 2004 as a high performance cathode material for SOFCs[7] with low polarization resistance in the intermediate temperature range 500−700 °C. An isothermal phase study for 1000 °C showed cubic phase, hexagonal phase, and other symmetries existing in the BSCF system depending on different Ba/Sr and Co/Fe ratios.[8] $Ba_{0.5}Sr_{0.5}Co_{0.8}Fe_{0.2}O_{3-\delta}$ exhibits a pure cubic phase at 1000 °C.[9] The temperature-dependent electrical conductivity of $Ba_{0.5}Sr_{0.5}Co_{0.8}Fe_{0.2}O_{3-\delta}$ exhibits a transition from semiconductivity to metal-like conductivity at 400−500 °C.[10−15] This transition is not due to any structural phase change.[16] However, only the long-term electrical conductivity of $Ba_{0.5}Sr_{0.5}Co_{0.8}Fe_{0.2}O_{3-\delta}$ at 800 °C slowly degrades, and a slow phase transformation from the cubic to mixed cubic, hexagonal, and hexagonal related phases at temperatures below 850 °C was reported in several studies of long-term phase stability.[17,18] Aside from the hexagonal phase, the formation of lamellar noncubic cobalt-rich phases was observed due to oxygen vacancy ordering, but the structure of these phases has not been completely resolved so far. As such, in some cases several micrometer-long lamellae are considered as barriers to oxygen transport due to their layered shape, low crystalline symmetry, and tiny amount of mobile oxygen vacancies.[19,20]

The electrical conductivity of $Ba_xSr_{1-x}Co_{0.8}Fe_{0.2}O_{3-\delta}$ (x = 0.3−0.7) decreases with increasing barium content.[21] Ba−rich BSCF compositions do not exhibit pure cubic phase at room temperature, for example, $Ba_{0.8}Sr_{0.2}Co_{0.8}Fe_{0.2}O_{3-\delta}$ is composed of mixed phases, one being cubic and others being hexagonal symmetry.[8] Early research predicted that Ba-rich BSCF compositions might undergo a phase transition from highly symmetric cubic to less symmetric hexagonal below 825−875 °C.[22] BSCF materials with the cubic phase exhibit good electrical conductivity at high temperatures, but degrade when being held at lower temperatures, i.e., below 800 °C and slowly transform from cubic to a hexagonal symmetry.[17] The phase relationships in this system lower than 1000 °C is still unclear.

In this work, we present the phase information of $Ba_{0.8}Sr_{0.2}Co_{0.8}Fe_{0.2}O_{3-\delta}$ using crystalline phase and microstructure analyses by X-ray diffraction (XRD) and transmission electron microscopy (TEM). The electrical conductivity and the thermal expansion of bulk materials show abrupt changes corresponding to the phase transition of $Ba_{0.8}Sr_{0.2}Co_{0.8}Fe_{0.2}O_{3-\delta}$.

Received: February 6, 2011
Revised: May 27, 2011
Published: June 17, 2011

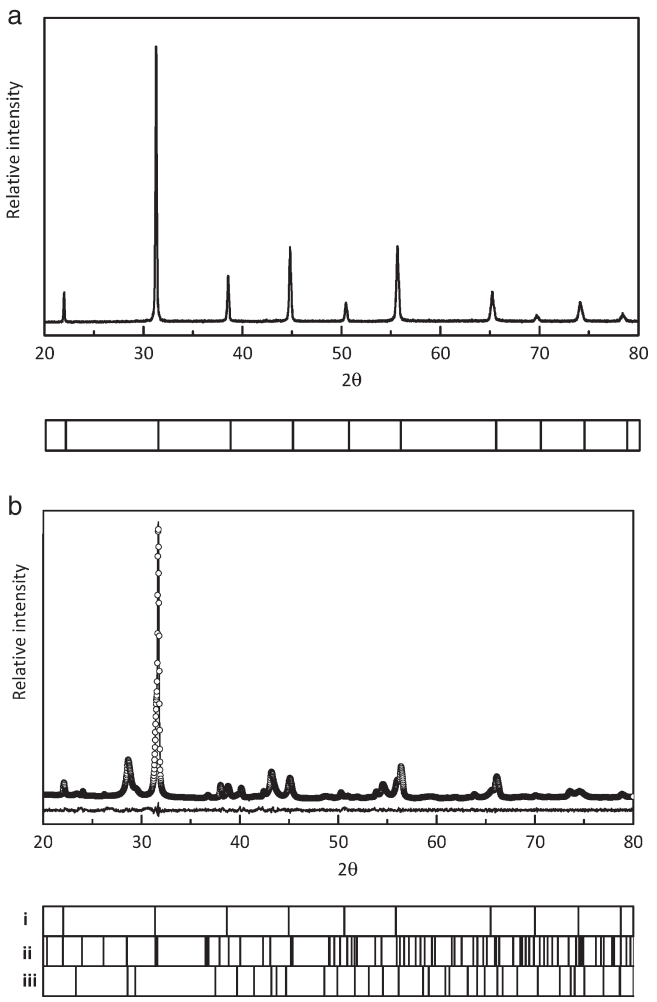

Figure 1. (a) XRD-pattern of the quenched powder specimen. The calculated Bragg-positions of the cubic perovskite phase are given at the bottom. (b) XRD-patterns of the furnace-cooled powder specimen: observed (solid line), calculated (points), and difference. The calculated Bragg-positions are given at the bottom of the figure for (i) cubic phase, (ii) hexagonal phase, and (iii) rhombohedral phase.

2. EXPERIMENTAL SECTION

Powder specimens of $Ba_{0.8}Sr_{0.2}Co_{0.8}Fe_{0.2}O_{3-\delta}$ were synthesized by the solid-state reaction method as described in detail in previous work.[8] The finely ground green powder was calcined at 1000 °C for 10 h in air. The crystalline phase of the calcined powder was identified by means of XRD. XRD data from the furnace-cooled and quenched-powder specimens were recorded on a Siemens Bruker D8 Advance X-ray diffractometer using Cu $K\alpha_{1,2}$ radiation in the $2\theta°$ range of 20°−80° with step sizes of 0.04° and of 0.02°, respectively. The phase analysis of the furnace-cooled specimen was carried out by combined Rietveld and Pawley methods using the TOPAS 4.0 (Bruker AXS) software. Because all observed phases exhibit related chemical compositions, we assume that the phases have similar X-ray mass absorption coefficients. Thus, the amounts of the phases can be estimated by calculating the areas of the corresponding phases in the XRD patterns using the Pawley method. The ratio of the areas of the integrated intensities delivers an approximate amount of the phase under consideration. The reliability of the method was controlled by XRD experiments on furnace-cooled powders using known amounts of $BaZrO_3$ as the internal standard. Calcined furnace-cooled powders were uniaxially pressed to shape the bulk specimen bars of 55 × 5 × 2.5 mm.[3] These green bars were cold isostatically pressed for 3 min at a pressure of 280 MPa and then sintered at 1100 °C for 6 h in air. A four-probe dc method was used to measure the electrical conductivity of the sintered specimen bars. Platinum wires (0.25 mm in diameter) were used as four electrodes glued to the sample with platinum paste for better contact. Keithley 2000 and 2001 multimeters together with self-programmed Labview software and a K-type thermocouple were used to record the experimental parameters of the specimen temperature and resistance. The sample was heated in a tube furnace with a ramp rate of 1 °C/min from room temperature up to 1060 °C with three heating and cooling cycles in air.

Differential thermal analysis and thermal gravimetry (DAT/TG) on powder and bulk specimens were performed as a function of temperature in synthetic air by mixing pure argon and pure oxygen (PanGas, 99.999% purity) gases in a DTA/TG (Netzsch STA 449 C). The heating and cooling rates were 1 °C/min. The thermal expansion of the same sintered bulk specimen bars after the electrical conductivity measurement was measured in air in a differential dilatometer (Baehr DIL 802) at a rate of 1 °C/min during heating and cooling cycles. TEM was used to characterize the furnace-cooled powder specimens that were heated at 1000 °C for 10 h. The microscope was a FEI Tecnai F30 operated at

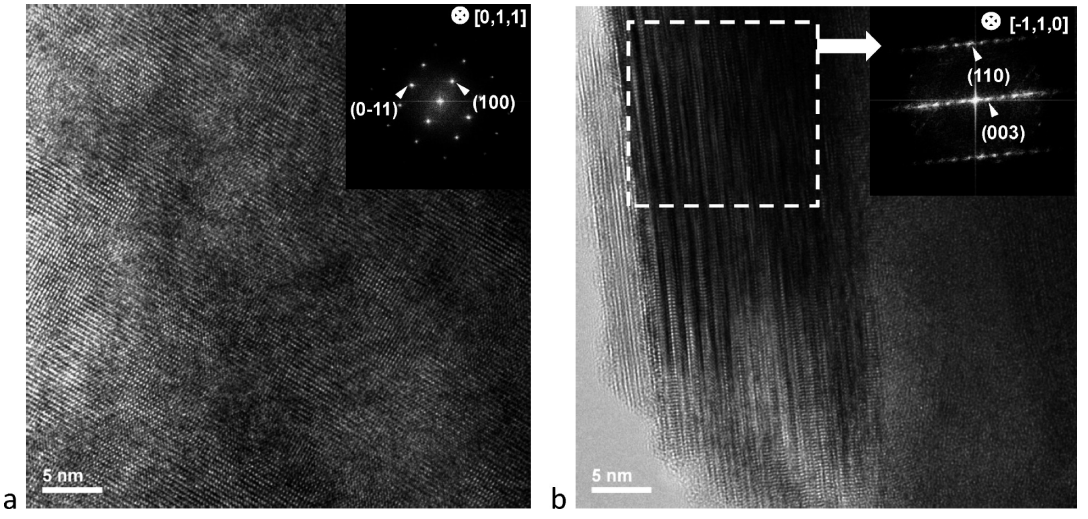

Figure 2. High-resolution transmission electron microscopy (HRTEM) images and diffraction patterns (insets) after fast Fourier transformation (FFT) calculations of the $Ba_{0.8}Sr_{0.2}Co_{0.8}Fe_{0.2}O_{3-\delta}$ calcined at 1000 °C for 10 h in air and then furnace cooled. (a) Cubic phase and (b) lamellar structure the rhombohedral phase coexisting in one grain with areas of cubic symmetry.

dx.doi.org/10.1021/cm200373r |*Chem. Mater.* 2011, 23, 3169–3175

300 kV with a postcolumn Gatan image filter (GIF), an EDAX SUTW Si (Li) detector, and a Phoenix EDAM III controller. The energy resolution was 134 eV. Some of the powder was mixed into 2 mL of ethanol and sonicated for 10 min to make a suspension. Drops of the suspension were applied from a pipet to a Cu TEM grid with perforated 100 holey carbon films. Images were collected in standard TEM mode and high-resolution (HRTEM). Energy-dispersive X-ray spectroscopy (EDXS) and mappings were taken in the scanning (STEM) mode with an electron-probe of about 2.5 nm in diameter.

3. RESULTS AND DISCUSSION

The powder specimen calcined at 1000 °C for 100 h in air exhibited different phases at room temperature. The quenched sample showed a pure cubic phase (Figure 1a), whereas the furnace-cooled specimen (∼-3 °C/min) exhibited a mixed phase (Figure 1b) at room temperature.

The phase analysis by combining Rietveld and Pawley methods (Figure 1b) shows that at least two additional phases besides the cubic phase (a = 4.044 Å) are present in the sample. Thus, a hexagonal phase (space group P63/mmc) with lattice parameters a = 5.657 Å and c = 28.434 Å as well as a rhombohedral phase (space group $R3m$; a = 5.825 Å and c = 37.157 Å) were deducted and included in the refinement by the Pawley fit. The mentioned phase symmetries are typical for the hexagonal perovskite polymorph as well as for hexagonal perovskite related barium cobalt oxides as described elsewhere.[20,23,24] Structure data for the known cubic perovskite phase were taken from the ICSD-database PDF 109462. The amounts of cubic phase of about 30%, hexagonal phase of about 40%, and rhombohedral phase of approximately 30% were estimated by considering the integrated scattering intensities of the respective phases. This mixed phase composition exists from room temperature up to 960 °C as evidenced by *in situ* high-temperature XRD[25] where the amount of cubic phase was found to increase with increasing temperature. The results show that a pure cubic phase of this material is preferred at temperatures above 960 °C. However, the cubic phase is not stable at temperatures below 960 °C for this composition. The fact that the fast cooling prevents the phase transition from cubic to hexagonal and that upon slow cooling this phase transition occurs indicate that it is diffusion controlled. High temperature *in situ* XRD analysis showed that these noncubic phases continue to develop at the expense of the cubic phase at lower temperatures.[25]

From HRTEM images of the powder specimen calcined at 1000 °C for 10 h in air and furnace cooled, a clear cubic phase (space group Pm-3 m; a = 4.044 Å; image viewed along the [0,1,1] direction, d(100) = a ≈ 4 Å and d(0−11) ≈ 2.9 Å, angle (100):(0−11) = 90° (Figure 2a)) and a lamellar structure rhombohedral phase (space group $R3\overline{m}$; a = 5.825 Å and c = 37.157 Å; image viewed along [−1,1,0] direction, d(003) = (1/3)c ≈ 12 Å and d(110) ≈ 2.8 Å, angle (003):(110) = 90° (Figure 2b)) were observed. Those lamellar shaped structures occur due to the partial transformation of the cubic BSCF phase to noncubic phases like the hexagonal and rhombohedral phases already found in the XRD patterns. Similar lamellar structures were found in the studies of Efimov et al. and Mueller et al. for the $Ba_{0.5}Sr_{0.5}Co_{0.8}Fe_{0.2}O_{3-\delta}$ composition.[19,20] Here, we have an insight into a nonequilibrium reaction sequence since the current sample was furnace cooled and not held in the intermediate temperature range for several hours as in the above-mentioned studies.

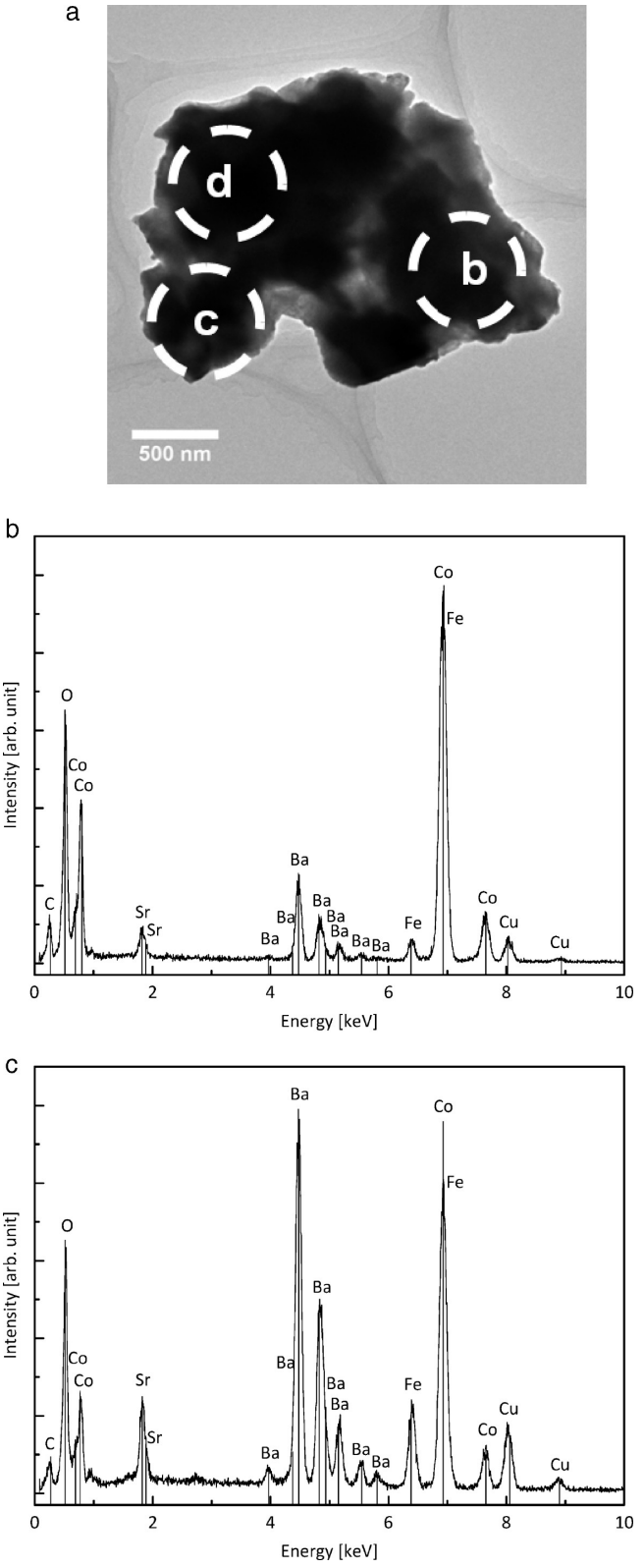

Figure 3. (a) TEM bright field image on three sites (b, c, and d) of one particle of the $Ba_{0.8}Sr_{0.2}Co_{0.8}Fe_{0.2}O_{3-\delta}$ powder calcined at 1000 °C for 10 h in air and furnace cooled. Panels b and c present the chemical elemental information by EDXS of site b and site c, respectively.

Figure 3 and Table 1 present chemical elemental information of three sites of one particle of the specimen giving the chemical

dx.doi.org/10.1021/cm200373r |*Chem. Mater.* 2011, 23, 3169–3175

stoichiometry of the metal ions by EDXS results. The nominal composition $Ba_{0.8}Sr_{0.2}Co_{0.8}Fe_{0.2}O_{3-\delta}$ is found on site c (Figure 3a, c and Table 1) and with a small deviation on side d (Figure 3a and Table 1). However, site b in Figure 3a shows a cobalt-rich composition (Figure 3a,b, and Table 1), which presumably is part of the more complex oxide phases leading to the multiple phase composition of the specimen.

In a detailed STEM high angle annular dark field (HAADF) micrograph in Figure 4, this cobalt-rich and Ba-/Sr-/Fe-depleted area is more pronounced. It becomes evident that the chemical constituents are not homogeneously distributed across the grain. The alkali earth deficient site b of the grain shows a higher Co concentration than the nominal composition. Combining the XRD data, we confirm that the crystalline phase of this composition after slow cooling to room temperature is not pure but that multiple phases exist in this specific composition, even locally in one grain. We can conclude that the Ba-rich composition $Ba_{0.8}Sr_{0.2}Co_{0.8}Fe_{0.2}O_{3-\delta}$ of the $Ba_xSr_{1-x}Co_yFe_{1-y}O_{3-\delta}$ system undergoes a phase transformation at intermediate temperatures with local demixing of the cations and ordering of the oxygen vacancies. With the ordering and disordering states of oxygen vacancies, many oxides show different phases from brownmillerite (ordering) to cubic (disordering) perovskite phase, e.g., Ca_2AlFeO_5,[26] Bi_2O_3,[27] $La_2Mo_2O_9$,[28] and $Ba_2In_2O_5$.[29] Here, an oxygen-vacancy-related phase transition was also found in the composition $Ba_{0.8}Sr_{0.2}Co_{0.8}Fe_{0.2}O_{3-\delta}$, in similar cobalt-containing perovskites,[30] and in $SrCo_{0.8}Fe_{0.2}O_{3-\delta}$.[31] A possible pathway of the transition from cubic perovskite to hexagonal has already been reported earlier.[19,20] The cubic ABO_3 perovskite consists of AO_3 layers arranged in cubic-close packing perpendicular to the [1,1,1] cubic zone axis. B-cations occupy the octahedral holes, and octahedra generate a three-dimensional corner-sharing array. The shear of some AO_3 layers inducted by the change of valence and spin-state of cobalt leads to the formation of hexagonal-close packing. Furthermore, the complex reconstructive transformations influenced by cation demixing occurred during the slow cooling of BSCF. Recently, Yi et al. reported high creep rates of

Table 1. Local Chemical Compositions of Each Site (b, c, and d) of Figure 3a by Showing Metal Ions in Atomic Percentage, on One Particle of the $Ba_{0.8}Sr_{0.2}Co_{0.8}Fe_{0.2}O_{3-\delta}$ Powder Calcined at 1000 °C for 10 h in Air and Furnace Cooled

	Ba (atm %)	Sr (atm %)	Co (atm %)	Fe (atm %)
nominal concentrations	40	10	40	10
b	14	4	78	4
c	39	11	39	11
d	36	12	41	11

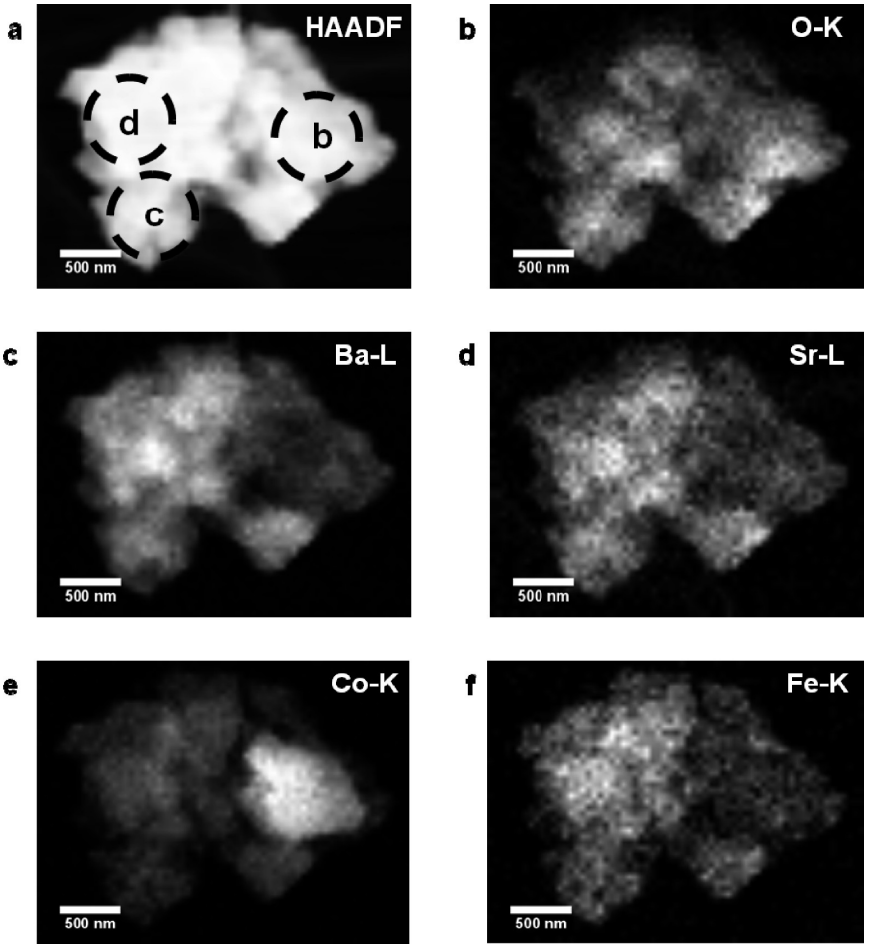

Figure 4. Scanning transmission electron microscopy (STEM) high angle annular dark field (HAADF) image (a) and the elemental distributions by EDX mapping (b–f) on the same particle of the $Ba_{0.8}Sr_{0.2}Co_{0.8}Fe_{0.2}O_{3-\delta}$ powder calcined at 1000 °C for 10 h in air and furnace cooled as shown in Figure 3.

dx.doi.org/10.1021/cm200373r |*Chem. Mater.* 2011, 23, 3169–3175

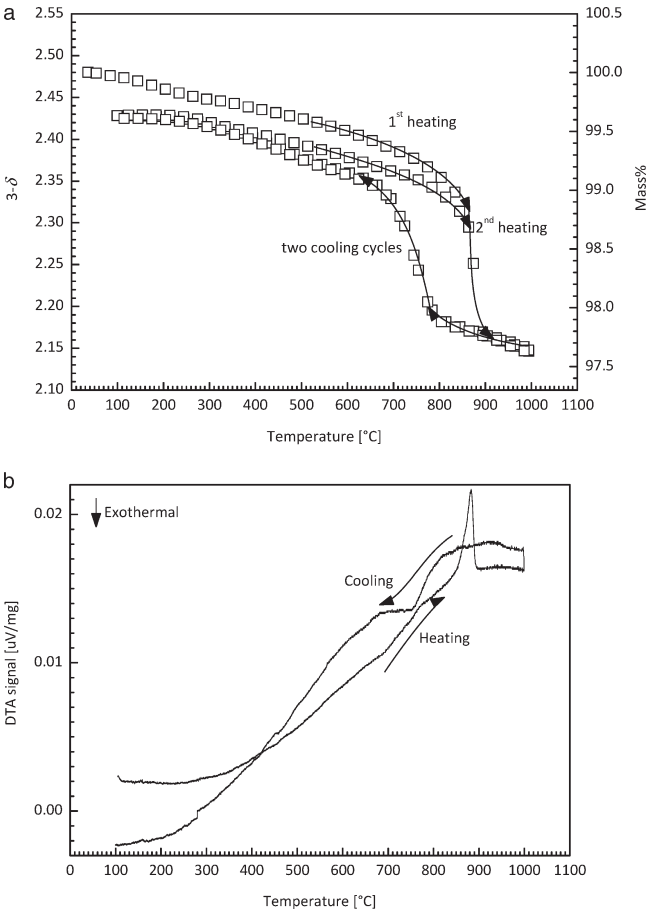

Figure 5. (a) Oxygen stoichiometry and (b) DTA signal of $Ba_{0.8}Sr_{0.2}Co_{0.8}Fe_{0.2}O_{3-\delta}$ as a function of temperature in synthetic air.

$Ba_{0.5}Sr_{0.5}Co_{0.8}Fe_{0.2}O_{3-\delta}$ controlled by cation diffusion.[32] Hence, high cation mobility delivers a possible explanation for the phase transition into compounds with nonperovskite compositions via complex pathways. However, we want to point out that the phase transformation is reversible in a rather short time of ca. 1 h as evidenced by the dilatometer measurements. As oxygen-vacancy mobility is rather fast in this material, the latter points toward a phase transformation due to the fast rearrangement of oxygen vacancies.

The change in oxygen content of the sintered bulk specimen (furnace cooled) during two heating and cooling cycles from room temperature to 1000 °C is shown in wt% in Figure 5. The initial oxygen content at room temperature was taken as $3-\delta = 2.48$ referenced from the similar composition $Ba_{0.5}Sr_{0.5}Co_{0.8}Fe_{0.2}O_{3-\delta}$ in the literature.[33] In the first heating cycle, the oxygen content of the sample continuously decreases with increasing temperature. An abrupt oxygen loss of 1 wt % was observed in a rather small temperature interval of 20 °C between 880 and 900 °C upon heating. During further heating, the sample further loses oxygen. Upon cooling from 1000 °C, the sample reoxidizes with decreasing temperature down to 800 °C when an abrupt oxygen gain occurs. With further cooling, more oxygen is incorporated into the material. The second thermal cycle shows behavior similar to that of the first thermal cycle including the hysteresis behavior in the temperature regime from 800 to 900 °C. The abrupt oxygen changes are accompanied by endo- and exothermic signals as shown in Figure 5b. Upon heating, the

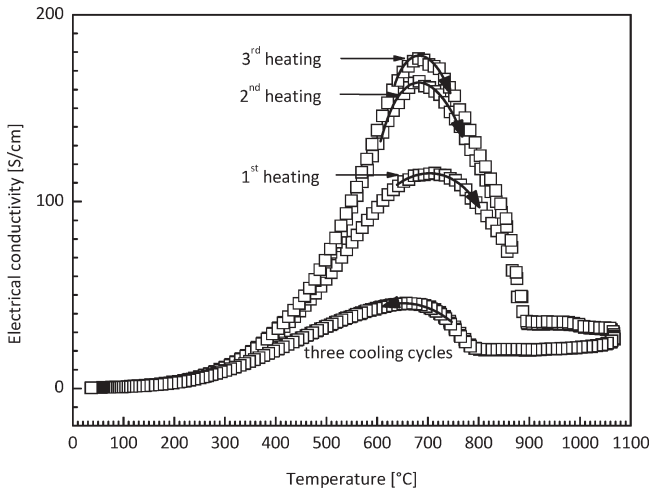

Figure 6. Electrical conductivity of the bulk specimen $Ba_{0.8}Sr_{0.2}Co_{0.8}Fe_{0.2}O_{3-\delta}$ in air at a rate of 1 °C/min. Note the discontinuity of the conductivity at 895 °C upon heating and at 790 °C upon cooling.

onset temperature is 855 °C, and an onset temperature is 820 °C for the exothermal event during cooling. Such a reversible phase transformation was already reported for a similar cobalt-containing oxide $BaSrCo_2O_5$ earlier.[34] The Fe-free $BaSrCo_2O_5$ transforms from a cubic symmetry below 900 °C into a rhombohedral phase upon cooling. The temperatures of endothermic and exothermic reactions are very similar for both $Ba_{0.8}Sr_{0.2}Co_{0.8}Fe_{0.2}O_{3-\delta}$ and $BaSrCo_2O_5$.

The electrical conductivity of a sintered bulk specimen bar (furnace cooled) as a function of temperature in air is shown in Figure 6 during three heating and cooling cycles. The electrical conductivity increases with increasing temperature, reaches a maximum at 670−710 °C, and then decreases upon further heating to 895 °C where a sharp discontinuity of the conductivity can be observed. The electrical conductivity does not change much with further heating up to 1060 °C. The discontinuity in electrical conductivity starts at 895 °C upon heating and at 790 °C during cooling. The maximum electrical conductivity occurs at 660 °C in the cooling cycles and increases with the number of cycles. During the cooling cycles, identical conductivities were observed. In the temperature range between room temperature and 660 °C, the material exhibits *p*-type semiconductivity, which can be described as a small polaron hopping mechanism at elevated temperatures.[13,15,35] It then undergoes a transition above 660 °C to metal-like conductivity. The latter can be understood when considering the increasing overlap of the transition metal *d* orbitals and oxygen *p* orbitals as already reported earlier.[15]

The sharp discontinuity in the conductivity upon heating at 895 °C correlates with the phase transitions from mixed hexagonal and rhombohedral phases to the cubic symmetry and is correlated with the abrupt oxygen loss at the same temperature shown in Figure 5a. The corresponding DTA signal (see Figure 5b) is endothermic. Obviously, oxygen vacancies are formed, and the transition metal cations (mainly Co) become reduced, changing their radii.[36] This leads to the phase change from mixed hexagonal and rhombohedral phases to the cubic symmetry. The state of oxygen vacancies, being ordered (rhombohedral and hexagonal phases) or disordered (cubic phase) in the lattice, obviously plays a crucial role in electrical conductivity and

dx.doi.org/10.1021/cm200373r |*Chem. Mater.* 2011, 23, 3169–3175

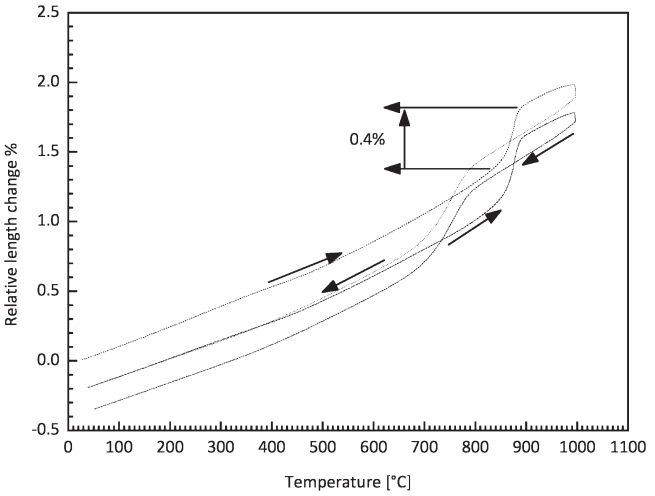

Figure 7. Relative length change of the bulk ceramic specimen of $Ba_{0.8}Sr_{0.2}Co_{0.8}Fe_{0.2}O_{3-\delta}$ as a function of temperature in air with two thermal cycles at a rate of 1 °C/min.

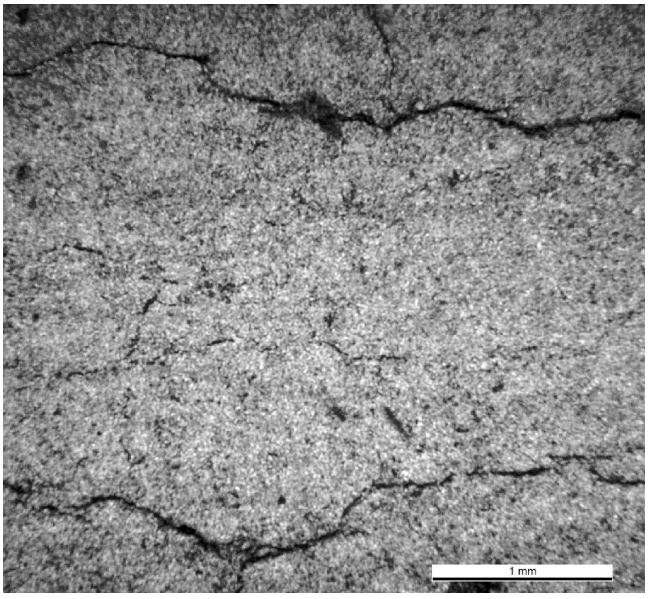

Figure 8. Microcracks in the $Ba_{0.8}Sr_{0.2}Co_{0.8}Fe_{0.2}O_{3-\delta}$ ceramic specimen bar predominantly running parallel to the long side of the specimen after 10 thermal cycles between room temperature and 1000 °C in air. (Optical micrograph, scale bar = 1 mm.)

presumably in oxygen ion conduction. However, the transition from ordered to disordered vacancy states cannot explain the discontinuity in the conductivity alone, e.g., at 895 °C, upon heating as is shown in Figure 6.

In order to elucidate this point further, we will now consider the relative length change of the ceramic specimen during heating and cooling cycles. Figure 7 shows the relative length change of the specimen during two subsequent heating and cooling cycles. Besides the usual length increase upon heating due to thermal and chemical expansion of 15.6×10^{-6} (1/°C), the material expands abruptly between 790 and 890 °C, with an onset at 850 °C during heating, and contracts upon cooling with an onset at 790 °C. The onset temperature becomes slightly shifted to higher temperatures during the second cycle. The abrupt length change is ±0.4% linear corresponding to 1.2 vol%. After thermal cycling, the specimen was still mechanically intact but exhibited many microcracks in the microstructure as is shown in the optical micrograph in Figure 8.

The redox-reaction of the transition metals between 700 and 900 °C causing the phase change leads to mechanical stresses exceeding the strength of the material and therefore causes the microcracks in the microstructure of the ceramic which were observed on the surface of $La_{0.5}Sr_{0.5}Co_{0.5}Fe_{0.5}O_{3-\delta}$ as well reported by Lein et al.[37] They attributed this mechanical fracture to the considerable stress gradients developing in the materials due to the gradient in oxygen concentration or the valence of Co.[37] Therefore, the crack formation reported here does not necessarily come due to the phase transition but might be caused by the considerable chemical expansion (oxidation of Co/Fe) during cooling. The hysteresis and the discontinuity of the electrical conductivity are a direct consequence of the disintegration of a coherent microstructure in this material.

4. CONCLUSIONS

The $Ba_{0.8}Sr_{0.2}Co_{0.8}Fe_{0.2}O_{3-\delta}$ composition of the $Ba_xSr_{1-x}Co_yFe_{1-y}O_{3-\delta}$ system shows a cubic symmetry (a = 4.044 Å) at 1000 °C when synthesized in air that can be retained in a metastable state at room temperature upon quenching. During slow cooling, the material transforms at 790 °C into a mixed phase state characterized by cubic, hexagonal, and rhombohedral symmetries. The latter exhibits a lamellar structure sometimes coexisting with areas of cubic symmetry in the same grain. The phase change is reversible and associated with the oxidation and reduction of the transition metal cations (mainly Co). The phase change is associated with a rather abrupt mass change of 1 wt % corresponding to a $\Delta\delta$ = 0.14 in the formula unit. The redox-reactions of the transition metal cations cause a reversible volume change of ~1.2 vol % of the bulk ceramic specimen leading to microcracks in the microstructure during thermal cycling. From room temperatures to ~670 °C, the material shows small polaron hopping p-type semiconductivity up to 180 S/cm, changing then to a metal-like conductivity. The conductivity is abruptly reduced by microcracks forming when the material transforms into the cubic symmetry at temperatures above 900 °C.

AUTHOR INFORMATION

Corresponding Author

*Tel: +41-44-633-68-53. Fax: +41-44-632-11-32. E-mail: zhen.yang@mat.ethz.ch.

ACKNOWLEDGMENT

We are grateful to Professor Joop Schoonman for helpful discussions. We acknowledge financial support by the Swiss National Science Foundation grant Scopes 2009-2012: JRP Project IZ73Z0_128185/1. We also acknowledge the support by the Electron Microscopy Center of ETH Zurich (EMEZ). K.E. thanks the State of Lower Saxony (Germany, NTH bottom-up project, No. 21-71023-25-7/09) for financial support.

REFERENCES

(1) Voorhoeve, R. J. H.; Johnson, D. W., Jr.; Remeika, J. P.; Gallagher, P. K. *Science* **1977**, *195*, 827–833.

(2) Bhalla, A. S.; Guo, R.; Roy, R. *Mater. Res. Innovations* **2000**, *4*, 3–26.
(3) Gauckler, L. J.; Beckel, D.; Buergler, B. E.; Jud, E.; Muecke, U. P.; Prestat, M.; Rupp, J. L. M.; Richter, J. *CHIMIA Int. J. Chem.* **2004**, *58*, 837–850.
(4) Minh, N. Q. *J. Am. Ceram. Soc.* **1993**, *76*, 563–588.
(5) Efimov, K.; Halfer, T.; Kuhn, A.; Heitjans, P.; Caro, J.; Feldhoff, A. *Chem. Mater.* **2010**, *22*, 1540–1544.
(6) Shao, Z.; Yang, W.; Cong, Y.; Dong, H.; Tong, J.; Xiong, G. *J. Membr. Sci.* **2000**, *172*, 177–188.
(7) Shao, Z.; Haile, S. M. *Nature* **2004**, *431*, 170–173.
(8) Yáng, Z.; Harvey, A. S.; Infortuna, A.; Gauckler, L. J. *J. Appl. Crystallogr.* **2009**, *42*, 153–160.
(9) Wei, B.; Lu, Z.; Li, S.; Liu, Y.; Liu, K.; Su, W. *Electrochem. Solid-State Lett.* **2005**, *8*, A428–A431.
(10) Zhao, H.; Shen, W.; Zhu, Z.; Li, X.; Wang, Z. *J. Power Sources* **2008**, *182*, 503–509.
(11) Jiang, G. S.; Song, C. L.; Li, D. C.; Feng, S. J.; Wei, L.; Chen, C. S. *Chin. J. Chem. Phys.* **2004**, *17*, 75–78.
(12) Zeng, P.; Chen, Z.; Zhou, W.; Gu, H.; Shao, Z.; Liu, S. *J. Membr. Sci.* **2007**, *291*, 148–156.
(13) Chen, Z.; Ran, R.; Zhou, W.; Shao, Z.; Liu, S. *Electrochim. Acta* **2007**, *52*, 7343–7351.
(14) Zhang, Y.; Liu, J.; Huang, X.; Lu, Z.; Su, W. *Solid State Ionics* **2008**, *179*, 250–255.
(15) Yáng, Z.; Harvey, A. S.; Infortuna, A.; Schoonman, J.; Gauckler, L. J. *J. Solid State Electrochem.* **2011**, *15*, 277–284.
(16) Wang, H.; Tablet, C.; Yang, W.; Caro, J. *Mater. Lett.* **2005**, *59*, 3750–3755.
(17) Svarcova, S.; Wiik, K.; Tolchard, J.; Bouwmeester, H. J. M.; Grande, T. *Solid State Ionics* **2008**, *178*, 1787–1791.
(18) Arnold, M.; Gesing, T. M.; Martynczuk, J.; Feldhoff, A. *Chem. Mater.* **2008**, *20*, 5851–5858.
(19) Mueller, D. N.; De Souza, R. A.; Weirich, T. E.; Roehrens, D.; Mayer, J.; Martin, M. *Phys. Chem. Chem. Phys.* **2010**, *12*, 10320–10328.
(20) Efimov, K.; Xu, Q.; Feldhoff, A. *Chem. Mater.* **2010**, *22*, 5866–5875.
(21) Wei, B.; Lu, Z.; Huang, X.; Miao, J.; Sha, X.; Xin, X.; Su, W. *J. Eur. Ceram. Soc.* **2006**, *26*, 2827–2832.
(22) Shao, Z.; Xiong, G.; Tong, J.; Dong, H.; Yang, W. *Sep. Purif. Technol.* **2001**, *25*, 419–429.
(23) Parras, M.; Varela, A.; Seehofer, H.; González-Calbet, J. M. *J. Solid State Chem.* **1995**, *120*, 327.
(24) Jacobson, A. J.; Hutchison, J. L. *J. Solid State Chem.* **1980**, *35*, 334.
(25) Harvey, A. S.; Litterst, F. J.; Yang, Z.; Rupp, J. L. M.; Infortuna, A.; Gauckler, L. J. *Phys. Chem. Chem. Phys.* **2009**, *11*, 3090–3098.
(26) Colville, A. A.; Geller, S. *Acta Crystallogr., Sect. B* **1971**, *27*, 2311–2315.
(27) Harwig, H. A.; Gerards, A. G. *J. Solid State Chem.* **1978**, *26*, 265–274.
(28) Lacorre, P.; Goutenoire, F.; Bohnke, O.; Retoux, R.; Laligant, Y. *Nature* **2000**, *404*, 856–858.
(29) Yoshinaga, M.; Yamaguchi, M.; Furuya, T.; Wang, S.; Hashimoto, T. *Solid State Ionics* **2004**, *169*, 9–13.
(30) Deng, Z. Q.; Yang, W. S.; Liu, W.; Chen, C. S. *J. Solid State Chem.* **2006**, *179*, 362–369.
(31) Liu, L. M.; Lee, T. H.; Qiu, L.; Yang, Y. L.; Jacobson, A. J. *Mater. Res. Bull.* **1996**, *31*, 29–35.
(32) Yi, J. X.; Lein, H. L.; Grande, T.; Yakovlev, S.; Bouwmeester, H. J. M. *Solid State Ionics* **2009**, *180*, 1564–1568.
(33) McIntosh, S.; Vente, J. F.; Haije, W. G.; Blank, D. H. A.; Bouwmeester, H. J. M. *Solid State Ionics* **2006**, *177*, 1737–1742.
(34) Boulahya, K.; Ruiz-Morales, J. C.; Hernando, M.; Gonzalez-Calbet, J. M.; Parras, M. *Chem. Mater.* **2009**, *21*, 2045–2054.
(35) Koc, R.; Anderson, H. U. *J. Eur. Ceram. Soc.* **1995**, *15*, 867–874.
(36) Shannon, R. *Acta Crystallogr., Sect. A* **1976**, *32*, 751–767.
(37) Lein, H.; Andersen, Ø.; Vullum, P.; Lara-Curzio, E.; Holmestad, R.; Einarsrud, M.-A.; Grande, T. *J. Solid State Electrochem.* **2006**, *10*, 635–642.